Thermal properties of the metallic delafossite PdCoO$_2$: A combined experimental and first-principles study

Yi Zhang (張易),[1] Amartyajyoti Saha [ORCID],[1,2] Fred Tutt [ORCID],[1] Vipul Chaturvedi,[1] Bryan Voigt,[1] William Moore,[1] Javier Garcia-Barriocanal,[3] Turan Birol [ORCID],[1] and Chris Leighton [ORCID][1,*]

[1]*Department of Chemical Engineering and Materials Science, University of Minnesota, Minneapolis, Minnesota 55455, USA*
[2]*School of Physics and Astronomy, University of Minnesota, Minneapolis, Minnesota 55455, USA*
[3]*Characterization Facility, University of Minnesota, Minneapolis, Minnesota 55455, USA*

Metallic delafossite materials (e.g., PdCoO$_2$, PtCoO$_2$), have attracted much recent attention due to record-high oxide conductivities, the origins of which remain unclear. Relatively little attention has been paid to their related *thermal* properties, however. We address this here via wide temperature range experimental studies of the crystal structure, thermal expansion, and specific heat of single-crystal PdCoO$_2$, combined with density-functional theory (DFT) calculations of the electronic and phononic densities of states, and thus thermal properties. PdCoO$_2$ is shown to retain the $R\bar{3}m$ space group from 12 to 1000 K, exhibiting $\underline{a}$- and $\underline{c}$-axis thermal expansion in good quantitative agreement with DFT-based lattice dynamics calculations. The Co-O bond lengths additionally elucidate the stability of the low-spin state of the nominally Co^{3+} ions, which is a notable difference between the edge-shared Co-O octahedra in PdCoO$_2$ and the corner-shared octahedra in Co-based perovskites. Measurements of specific heat from 1.9 to 400 K provide accurate values for the Debye temperature and Sommerfeld coefficient, the phononic part being describable via a combined Debye-Einstein approach (accounting for high-frequency oxygen-related optical phonons), with excess intermediate-temperature specific heat due to a prominent low-energy peak in the phonon density of states. Most significantly, all electronic and phononic contributions to the specific heat are shown to be remarkably closely reproduced by DFT-based calculations, establishing quantitative understanding of key thermal properties of the metallic delafossite PdCoO$_2$.

I. INTRODUCTION

A sizable number of complex oxides are known to crystallize in the delafossite structure, with ABO_2 stoichiometry [1–4]. The A^{1+} ions in this family crystallize in two-dimensional (2D) triangular sheets, forming linearly coordinated bonds with adjacent O ions in edge-shared $B^{3+}O_6$ octahedra, thus creating highly anisotropic layered structures [Figs. 1(a)–1(c)] [2,4]. The majority of such delafossites are insulators or semiconductors, prominent examples being the CuFeO$_2$ and related materials that have been studied in the context of frustrated magnetism [5–8], and for various energy applications [9–12]. A smaller number of delafossites are metallic, most notably PdCoO$_2$, PtCoO$_2$, PdCrO$_2$, and PdRhO$_2$ [1–4,13]. These materials, with formally monovalent Pd or Pt, and trivalent Co, Cr, or Rh, have been known since 1971 [1–3] but have only recently been recognized to exhibit extraordinary properties [4,13]. Specifically, PdCoO$_2$ and PtCoO$_2$ are now understood to be *the most conductive oxides known* [4]. Their in-plane [i.e., $\underline{a}$-$\underline{b}$ plane; see Figs. 1(a)–1(c)] room-temperature resistivities have been reported to be 3.1 and 1.8 $\mu\Omega$ cm, respectively [14], comparable to or less than Au. Equally remarkably, their residual resistivities fall as low as 8 nΩ cm [14], generating residual resistivity ratios

approaching 400 [14,15]. Such low-temperature resistivities imply electron mobilities up to $\sim$34 000 cm^2 V^{-1} s^{-1} and mean-free-paths up to $\sim$20 μm [4,16], despite their three-component complex-oxidic nature, and 2D structures. This suggests an extraordinary level of purity and crystalline perfection [17,18], or some source of insensitivity to defects and scattering, the origins of which are unclear [4].

The electronic structure of the metallic delafossites is equally remarkable. Continuing to use the most extensively studied PdCoO$_2$ and PtCoO$_2$ as examples, these materials have been shown, from experiment [15,16,19–24] and theory [22,25–32], to exhibit strikingly simple electronic structure. A single Pd- or Pt-d band crosses the Fermi level (E_F), the electron effective masses are only 1.1–1.5 m_e, and the Fermi surface is a hexagonal cross-section cylinder filling half the first Brillouin zone [15–30] [Figs. 1(d) and 1(e)]. Additionally, the formally Co^{3+} ions are thought to be in a low-spin ($S = 0$) configuration, while the Pd- or Pt-derived itinerant electrons generate relatively simple Pauli paramagnetism [4,15,33,34]. These compounds thus realize near-ideal nearly free-electron behavior in nonmagnetically-ordered 2D systems [20], enabling a series of exciting advances. As already alluded to, state-of-the-art residual resistivity ratios, deduced mobilities, and extracted mean-free paths have reached almost 400, $\sim$34 000 cm^2 V^{-1} s^{-1}, and $\sim$20 μm, respectively, with $\underline{c}$-axis/$\underline{a}$-$\underline{b}$-plane resistivity anisotropies of >100 [4,15,16]. Such crystals have been utilized in recent observations of
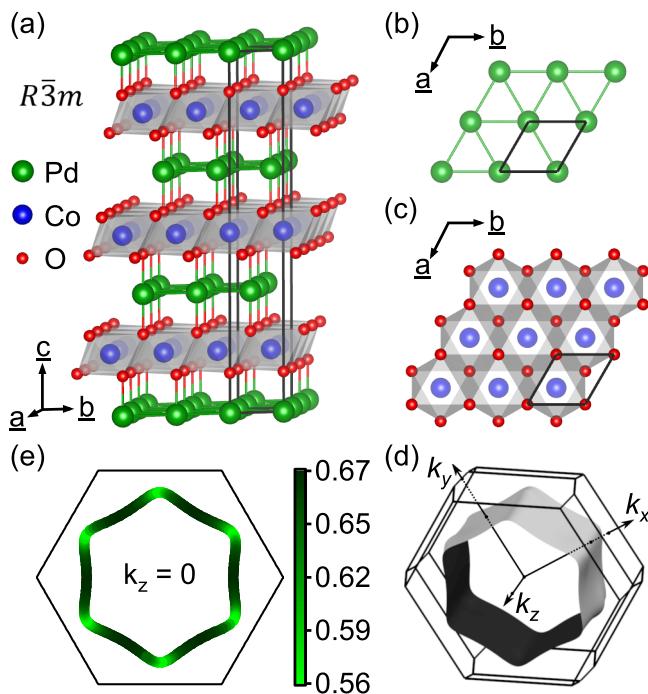
_____

*leighton@umn.edu

FIG. 1. (a) Three-dimensional rendering of the room-temperature crystal structure of $R\bar{3}m$ PdCoO$_2$. Pd, Co, and O ions are shown in green, blue, and red, respectively, and the crystal axes $\underline{a}$, $\underline{b}$, and $\underline{c}$ are defined. (Illustrations were generated in VESTA [97] from the structure file in Ref. [80]). (b) and (c) illustrate the $\underline{a}$-$\underline{b}$-plane arrangements of Pd ions and edge-sharing Co-O octahedra, respectively. A single hexagonal unit cell ($a = 2.83$ Å, $c = 17.743$ Å at room temperature) is outlined. (d) Three-dimensional DFT-calculated PdCoO$_2$ Fermi surface within the first Brillouin zone (black lines) of the rhombohedral unit cell (plotted with XCRYSDEN [98]). (e) Two-dimensional DFT-calculated $k_z = 0$ Fermi surface cut within the first Brillouin zone (black line) of the hexagonal lattice. The shades of green correspond to the fractional weight of the Pd-d orbital contribution, relative to the sum of the Pd, Co, and O s, p, and d orbitals.

quantum oscillations (de Haas–van Alphen and Shubnikov–de Haas) [15,16,23,24], enormous $\underline{c}$-axis positive magnetoresistance for specific in-plane magnetic field directions [35], unconventional $\underline{a}$-$\underline{b}$-plane magnetoresistance [14], exponentially temperature-dependent resistivity implicating phonon drag effects [16], supergeometric electron focusing effects associated with the hexagonal Fermi surface [36], potential hydrodynamic electron transport [23], and itinerant surface ferromagnetism [22,37,38]. Various groups are also grappling with the origins of the record conductivity, through the deliberate introduction of defects [18], and via insights into how the unique electronic structure could mitigate impurity scattering [32]. Numerous thin-film synthesis efforts are also underway [37,39–51].

Understandably, the focus of the majority of the above results is firmly on transport, meaning that far less is understood regarding other properties of metallic delafossites, including structural and thermal. It appears unknown, for example, whether bulk PdCoO$_2$ and PtCoO$_2$ retain their room-temperature $R\bar{3}m$ structure to lower and higher temperature (T), or whether structural transformations or anomalies occur. The latter are well known in Co^{3+}-based perovskites, due to spin-state crossovers from the low-spin state [52–59]. The thermal expansion of metallic delafossites is also unexplored, even though nonmetallic delafossites exhibit anomalous thermal expansion tendencies, including regimes of negative thermal expansion [60,61]. Knowledge and understanding of the specific heat (C_P) of metallic delafossites is similarly limited, despite that the electronic contribution to C_P provides direct insight into the electronic structure, while the phononic contribution is directly relevant to the phonon scattering that impacts the extraordinary T-dependent resistivity. In more detail, the first report of $C_P(T)$ in PdCoO$_2$ focused on the low-T regime only, deducing a Debye temperature (Θ_D) of 456 K and a Sommerfeld coefficient (γ) of 4.14 mJ mol^{-1} K^{-2} [62]. The latter is now understood to be in poor quantitative agreement with the electronic structure [4], however, while a large, potentially impurity-related [4,15] Schottky anomaly was also found [62]. Subsequent $C_P(T)$ measurements were performed over a wider T range, on higher-quality crystals [4], yielding a quite different γ of 1.28 mJ mol^{-1} K^{-2} and a low-T Θ_D of 501 K [15]. The higher-T behavior was shown to be describable within a Debye-Einstein approach with $\Theta_D = 340$ K and Einstein temperature $\Theta_E = 790$ K [15]. Various features known to arise in the $C_P(T)$ of other compounds with BO_6 octahedra, such as excess specific heat associated with low-energy peaks in the phonon density of states [63], have also not been observed in PdCoO$_2$ or PtCoO$_2$. There thus exist a host of open issues that could potentially be elucidated via a systematic study of thermal properties of PdCoO$_2$ or PtCoO$_2$, particularly if performed on high-quality single crystals.

This work addresses the above through a wide-range (12–1000 K) T-dependent study of the crystal structure of PdCoO$_2$, as well its $\underline{a}$- and $\underline{c}$-axis thermal expansion, via x-ray diffraction (XRD). This is augmented with a wide-range (1.9-400 K) $C_P(T)$ study, all on high-quality crystals, closely correlated with first-principles calculations *via* density-functional theory (DFT). The structural studies reveal that the $R\bar{3}m$ space group is retained over the entire T range, with no structural transformation, and with $\underline{a}$- and $\underline{c}$-axis thermal expansion in good quantitative agreement with DFT-based lattice dynamics calculations. Co-O bond lengths additionally provide insight into the stability of the low-spin state of the nominally Co^{3+} ions in the edge-shared Co-O octahedra of PdCoO$_2$, in contrast to the corner-shared Co-O octahedra in perovskite cobaltites. Careful analysis of the low-T $C_P(T)$ yields accurate values for the low-T Θ_D and γ of 523 K and 1.16 mJ mol^{-1} K^{-2}, respectively, the latter being in quantitative agreement with the electronic structure. Consistent with Takatsu *et al.* [15], the broader-T range $C_P(T)$ can be modeled within a Debye-Einstein approach, where the Debye term (with $\Theta_D = 360$ K) captures the Co- and Pd-related phonon modes, while the Einstein term (with $\Theta_E = 830$ K) captures O-related high-frequency optical modes. We also detect excess intermediate-T phononic C_P associated with the first peaks in the PdCoO$_2$ phonon density of states (DOS), which can be crudely captured with an additional Einstein mode with $\Theta_E = 180$ K. Moreover, each of these electronic and phononic contributions to C_P is shown to be remarkably well

reproduced by DFT calculations. We thus conclude *quantitative* understanding of key thermal properties of the prototype delafossite metal $PdCoO_2$, advancing the understanding of this fascinating materials class.

II. EXPERIMENTAL AND COMPUTATIONAL DETAILS

$PdCoO_2$ crystals were grown using a two-step process. First, high-purity $PdCoO_2$ precursor powder was prepared via the metathesis reaction $PdCl_2 + Co_3O_4 + Pd \rightarrow 2PdCoO_2 + CoCl_2$ [1]. For this, high-purity $PdCl_2$ (Alfa Aesar, 99.999%), Co_3O_4 (Alfa Aesar, 99.9985%), and Pd (Sigma-Aldrich, 99.995%) powders were thoroughly mixed and loaded into quartz ampoules in a 1.5:1:1 molar ratio, the additional $PdCl_2$ being reported to promote $PdCoO_2$ crystallization [15]. The ampoules were vacuum sealed (at $\sim 10^{-6}$ Torr) then heated at $300\,°C/h$ to $750\,°C$ in a box furnace, held at $750\,°C$ for 60 h, cooled at $40\,°C/h$ to $400\,°C$, and furnace cooled to room temperature. The product was then successively washed in boiling ethanol and room-temperature acetone, to remove excess chlorides. Powder XRD revealed minor Pd and Co_3O_4 phase impurities at this stage. In the second step, chemical vapor transport (CVT) was used to grow $PdCoO_2$ crystals, informed by prior Cl-based CVT of PdO and Co_3O_4 [64]. For this, ~ 1 g of the $PdCoO_2$ precursor was loaded and vacuum sealed (at $\sim 10^{-6}$ Torr) in a second quartz ampoule with ~ 0.1 g of $PdCl_2$ powder (Alfa Aesar, 99.999%). The ampoule was then placed in a two-zone furnace, with hot and cold zones at 760 and $710\,°C$. After a 3-d inversion period to clean the growth zone, the growth was run for 13 d. As we will detail elsewhere [65], CVT likely proceeds via $PdCoO_2(s) + 2Cl_2(g) \leftrightarrow PdCl_2(g) + CoCl_2(g) + O_2(g)$. In essence, decomposition of the precursor $PdCl_2$ produces Cl_2, which reacts with $PdCoO_2$ to form $PdCl_2$, $CoCl_2$, and O_2, all in the gas phase, enabling the above reaction to run to the left (in the cold zone), growing high-purity $PdCoO_2$ crystals. Multicrystals with up to 12-mm lateral dimensions and several millimeter thickness were routinely grown; as demonstrated below, sizable single crystals were readily obtained from these multicrystals.

Final crystals were characterized by room-temperature powder x-ray diffraction (PXRD) (on powdered crystals), 2D area-detector XRD, and high-resolution XRD (HRXRD). These measurements utilized a Rigaku Miniflex diffractometer (Cu $K\alpha$), a Bruker D8 Discover diffractometer (Co $K\alpha$), and a Rigaku Smartlab XE diffractometer (Cu $K\alpha$), respectively. Energy-dispersive x-ray spectroscopy (EDS) was also performed, in a JEOL JSM-6010PLUS/LA scanning electron microscope (at 20 kV) with an integrated EDS detector. T-dependent PXRD data were collected on a Rigaku Smartlab SE diffractometer with an Oxford Cryosystems PheniX closed-cycle cryostat from 12 to 293 K (in vacuum, through a Kapton window), and on a Rigaku Smartlab XE diffractometer with an Anton Paar DHS 1100 graphite-domed hot stage from 293 to 1000 K (in air), both using Cu $K\alpha$. In the latter case, a 2D detector was employed and Rigaku SMARTLAB software was used to reduce the data to 1D profiles. Rietveld refinements (using MDI JADE software) were then performed at each T to extract the a- and c-lattice parameters, and other structural

details; in the high-temperature case, peaks from the graphite dome were excluded. $C_P(T)$ measurements (1.9–400 K) were made in a Quantum Design Physical Property Measurement System (PPMS) using relaxation calorimetry. Apiezon grease was used to affix crystals to PPMS platforms (Apiezon N from 1.8 to 250 K and Apiezon H from 200 to 400 K), 2% temperature pulses were used, the sample thermal coupling was above 95% at all T, and the sample-to-addenda heat-capacity ratio was maintained above a minimum of 0.7 [66].

First-principles calculations were performed using DFT with the projector augmented-wave formalism, as implemented in the Vienna *Ab initio* Simulation Package (VASP) [67,68], using the accepted room-temperature structural parameters [1–3]. The exchange-correlation energy was approximated using the Perdew-Burke-Ernzerhof generalized gradient approximation revised for solids (PBEsol) [69]. The energy cutoff for the plane waves was set to 500 eV, and spin-orbit coupling was not accounted for (it was found to be insignificant near E_F). Electronic band structure and DOS calculations were done with the room-temperature experimental structure [2], on a Γ-centered Monkhorst-Pack grid [70] of $16 \times 16 \times 16$ k points for the Brillouin zone of the primitive cell. The orbital characters of the electronic wave functions and DOS were obtained from atomic spheres, renormalized to account for interstitial densities. To accurately calculate the electronic DOS near E_F to extract the Sommerfeld coefficient, the WANNIER90 package [71,72] was used to calculate maximally localized Wannier functions and interpolate the electronic structure on a $400 \times 400 \times 400$ k-point grid. The splitting between Co t_{2g} and e_g orbitals was also calculated from the difference of the average on-site energies of the Wannier orbitals. This calculation was done as a function of temperature, using the temperature-dependent structural parameters determined in this work. While there are internal splittings in both the t_{2g} and e_g orbitals, due to the site symmetry and numerical noise, these were much smaller than changes due to the crystal structure and were thus ignored.

Phonon calculations were performed using the direct approach as implemented in the PHONOPY package [73], typically on a $2 \times 2 \times 2$ supercell (one set of calculations was run using a $3 \times 3 \times 3$ supercell, as discussed below). In this approach, symmetry is used to determine the smallest number of displacements required to obtain all force constants commensurate with a supercell, ions are displaced accordingly, and forces are calculated using self-consistent DFT calculations for each displacement pattern. A Γ-centered Monkhorst-Pack grid of $8 \times 8 \times 8$ k points was used for these electronic structure calculations in the supercell. Phonon frequencies were typically calculated on a $128 \times 128 \times 128$ k-point grid, using the force constants obtained from the $2 \times 2 \times 2$ supercell, which was then used to calculate the phonon band structure, phonon DOS, and phonon specific heat. Thermal expansion coefficients were calculated within the quasiharmonic approximation, using the Grüneisen theory of thermal expansion [74], with a fully relaxed structure. The extracted thermal expansion coefficients were then used along with the 12 K experimental lattice parameters to calculate the T-dependent lattice parameters.

III. RESULTS AND ANALYSIS

We first present the results of DFT calculations of the electronic and phononic structures of PdCoO$_2$ (Sec. III A), followed by room-temperature structural characterization of single crystals (Sec. III B). This is followed by a discussion of T-dependent PXRD and the associated extracted thermal expansion and bond lengths (Sec. III C), then specific-heat data and analysis (Sec. III D).

A. First-principles calculations

As already noted, Figs. 1(a)–1(c) depict the accepted experimentally determined room-temperature crystal structure of PdCoO$_2$ (space group $R\bar{3}m$, with the a- and c-lattice parameters in the caption [2]). Figure 1(a) provides a 3D rendering (with a hexagonal unit cell marked), Fig. 1(b) shows the Pd arrangement in the a-b planes, and Fig. 1(c) shows the Co-O octahedra arrangement in the a-b planes. All Pd layers have the same a-b plane arrangement, but are staggered in a three-layer sequence [Fig. 1(a)], generating a rhombohedral $3R$-type formation [4], and thus space group $R\bar{3}m$.

Our DFT-calculated electronic structure based on this structure is in generally good agreement with prior work [22,25–32]. Figure 1(d) shows the calculated Fermi surface, which consists of a single Γ-centered pocket, in line with earlier calculations [25,26,29–32]. While this pocket is approximately hexagonal, some corrugation occurs along the k_z axis, consistent with the $\bar{3}m$ symmetry. Following from the discussion in Sec. I, we indeed find low-spin formally Co^{3+} ions, with completely filled t_{2g} orbitals and empty e_g orbitals, whereas the formally Pd^{1+} ions have single holes in their d orbitals. The single band in Fig. 1(d) thus appears to derive from Pd-d orbitals. Figure 1(e) depicts the wave-function character projected on the $k_z = 0$ plane, revealing, however, that while the orbital character of the Fermi surface is indeed Pd-d dominated, there are significant contributions from Co, and associated orbital character variations in the k_x-k_y plane. The low-energy electronic structure is further elucidated in Fig. 2(a), which shows the electronic band structure, including projections of the Bloch wave functions onto Pd-d, Co-d, and O-p orbitals. The O bands reside well below E_F and have no significant contribution to the Fermi surface. The Co t_{2g}- and e_g-derived bands straddle E_F, however, the former overlapping and mixing heavily with Pd-d bands, meaning that the half-filled band crossing E_F has significant Co character. At certain k vectors this band in fact has higher contribution from Co than Pd, although it is Pd dominated at E_F. The band structure in Fig. 2(a) results in the atomically- and orbitally-projected DOS in Fig. 2(b), which further supports the above. In particular, at E_F, the Pd-d contribution to the total DOS is largest, but with a significant Co-d contribution, while, unlike in most late transition-metal oxides, the O contribution is low.

Figures 2(c) and 2(d) present the corresponding calculated phononic band structure and DOS, again atomically projected, using red for O, blue for Co, and green for Pd. [Note that there are multiple approaches to such color schemes. In Fig. 2(c) we use a linear one based on the sums of the squares of the dynamical matrix components for each ion; this is discussed more fully and compared to an alternative approach based on squared atomic displacements in Supple-

mental Material [75], Fig. S1 and the associated caption.] As in many transition-metal oxides (e.g., BaTiO$_3$, PbZrO$_3$ [76,77]), and indeed insulating delafossites (e.g., CuFeO$_2$, CuCrO$_2$ [78,79]), the highest-frequency phonon branches are dominated by O displacements [red in Figs. 2(c) and 2(d)], due to the low atomic mass. Strikingly, however, in PdCoO$_2$ this high-frequency manifold (which was previously detected in Raman spectroscopy [15]) is essentially completely distinct from the rest of the phonon band structure, via a gap of ~1 THz beginning at ~12.5 THz. All six phonon bands associated with O displacements reside in this high-frequency manifold. The Co- and Pd-derived phonon bands [blue and green in Figs. 2(c) and 2(d)] then populate the region below ~12.5 THz, with some overlap and mixing. As is necessary, the color of the lines in Fig. 2(c) thus becomes fully mixed as the Γ point is approached, as long-wavelength lattice vibrations of course involve all atoms. As returned to in Sec. III D, one can then appreciate from Fig. 2(d) that the phononic DOS of PdCoO$_2$ might be crudely described using a Debye model to capture the Co and Pd DOS [see the lower dashed line in Fig. 2(d), with Debye frequency $\omega_D = k_B \Theta_D / \hbar \approx 11$ THz], along with an Einstein model to capture the relatively narrow higher-energy O DOS [see the higher dashed line in Fig. 2(d), with Einstein frequency $\omega_E = k_B \Theta_E / \hbar \approx 17.5$ THz]. This combination will be shown below to indeed provide a good description of $C_P(T)$.

As an aside, we note that the separation of O-related phonons from the rest of the lattice vibrations [Figs. 2(c) and 2(d)], in conjunction with the layered structure [Fig. 1(a)], suggests that the phononic structure of PdCoO$_2$ could be considered essentially 2D. We mean by this that the vibrations of a given layer of O ions are to a substantial extent decoupled from neighboring layers of O ions. This is corroborated by the relatively low bandwidth of the optical phonon branches (particularly those with O character) between the Γ- and T points of the Brillouin zone, where only the out-of-plane wave vector is nonzero. [Compare the dispersion of the O modes between Γ and T in Fig. 2(c), i.e., along k_z (see Fig. 2(b), inset) with the dispersion in other directions]. One could then speculate on the relation of this feature to a specific aspect of the behavior of PdCoO$_2$ and PtCoO$_2$, namely the absence of superconductivity down to 15 mK [15]. While the influence of this type of phonon behavior on superconductivity is not yet clear, this is clearly worthy of further exploration, as the absence of superconductivity in these compounds is surprising given their high electronic DOS at E_F and lack of magnetic order. Calculations of electron-phonon coupling would also be of clear interest.

B. Room-temperature structural characterization

We begin the experimental part of this paper with room-temperature structural and chemical characterization of our crystals. Figure 3(a) first shows a photograph of an example single-crystal (~6 × 4 mm) surface, isolated from a CVT-grown multicrystal. Single crystallinity is supported by the 2D XRD data in Fig. 3(b) (showing three stitched 2D detector images), which reveal only the 0 0 3, 0 0 6, 0 0 9, and 0 0 12 reflections, consistent with an 0 0 1-oriented crystal. The PXRD data in Fig. 3(c) were obtained from a powdered sample of
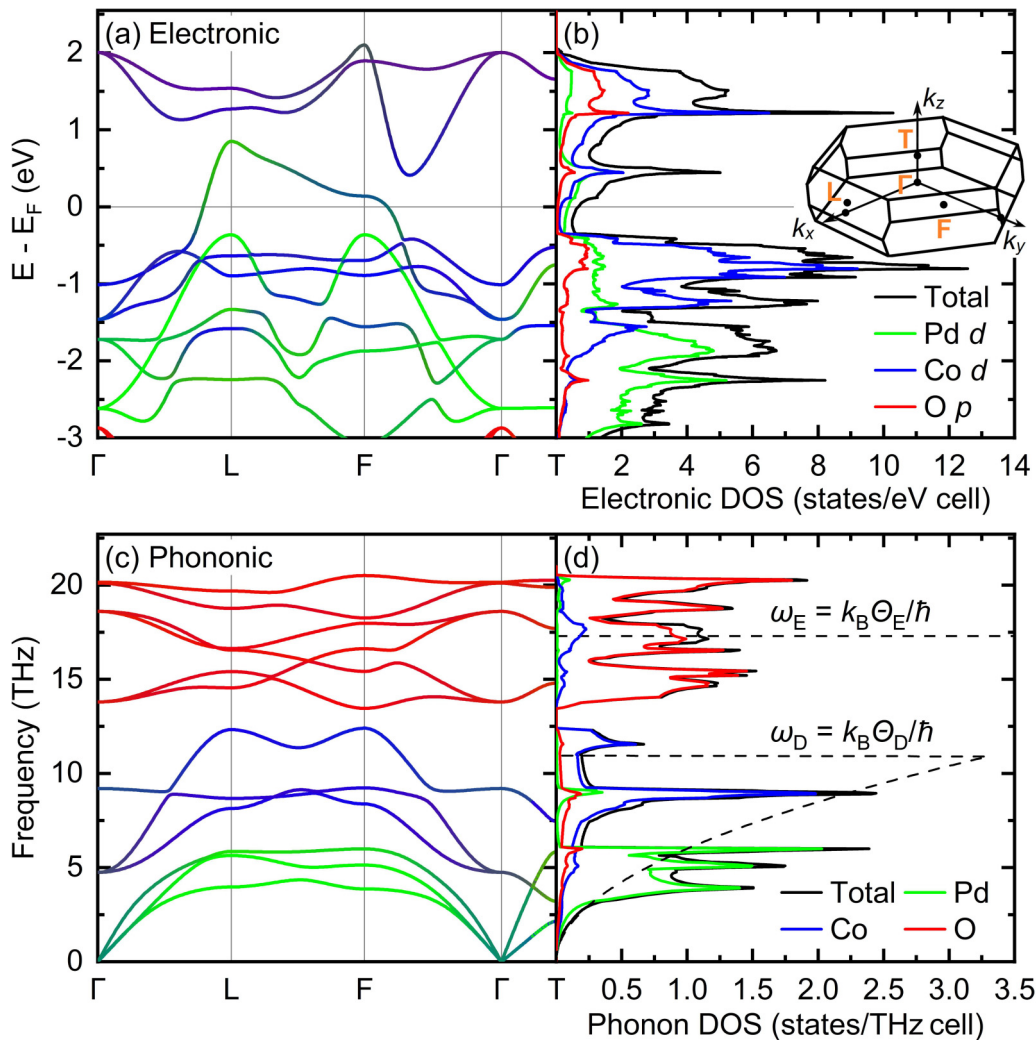
FIG. 2. DFT-calculated electronic and phononic band structures (a), (c) and electronic and phononic DOS (b), (d) of PdCoO$_2$. Using methods described in the text, both the band structures and densities of states are denoted with their Pd (green), Co (blue), and O (red) character. The inset to (b) depicts the first Brillouin zone of the rhombohedral lattice, with the high-symmetry points Γ, L, F, and T labeled. The dashed lines in (d) illustrate the Debye DOS and frequency (ω_D), and the Einstein frequency (ω_E), based on the low-T Debye temperature [from Fig. 6(b)], and the Einstein temperature from the 1.9–400 K Debye-Einstein fit to the specific heat [from Fig. 6(a)], respectively.

such crystals, the similarity with the PdCoO$_2$ reference pattern [80] being striking, both in terms of peak positions and intensities; no unassigned peaks arise. This evidences phase-pure delafossite PdCoO$_2$, as reinforced below by Rietveld refinements of such PXRD data. Figure 3(d) then shows an HRXRD specular θ-2θ scan from a single crystal, for comparison with the powdered crystal in Fig. 3(c). Only the 0 0 l family of peaks are seen in Fig. 3(d), further confirming single crystallinity. The inset to Fig. 3(d) shows a rocking curve through the 0 0 6 single-crystal reflection. While multiple peaks are seen, likely related to the nonideal nature of the crystal surface [Fig. 3(a)], the width of the primary rocking-curve peak is only 0.03 °. This indicates low absolute mosaicity, although we are unaware of any other reports of PdCoO$_2$ single-crystal mosaic spread to compare to. Finally, EDS data on these crystals reveal only Pd, Co, and O peaks (aside from usual surface contamination species, e.g., C), a typical extracted Pd/Co atomic ratio being 0.98 ± 0.05. This further supports nominally stoichiometric PdCoO$_2$.

C. Temperature-dependent structural measurements

PXRD data of the type shown in Fig. 3(c) were obtained from 12 to 1000 K, using a combination of a cryostat and a furnace stage, as described in Sec. II. The 12 K pattern (black) is shown in Fig. 4(a), along with the result of a Rietveld refinement (blue), the resulting difference (pink) being shown in the panel below. The obtained χ^2 values were $\sim$1–1.5 below room temperature, rising to 4–8 at the highest temperatures. The refinement is based on ideally stoichiometric PdCoO$_2$ in the $R\bar{3}m$ space group, resulting in $a = 2.8264 \pm 0.0002$ Å and $c = 17.739 \pm 0.002$ at 12 K. No structural transformations from this space group were detected to the maximum temperature (1000 K), indicating that the 3R delafossite polymorph is stable at all relevant T under these conditions. We stress that these high-T PXRD data were acquired in air, where the PdCoO$_2$ decomposition temperature should exceed 1000 K [1,47]; decomposition at a significantly lower T was found in vacuum, as expected.
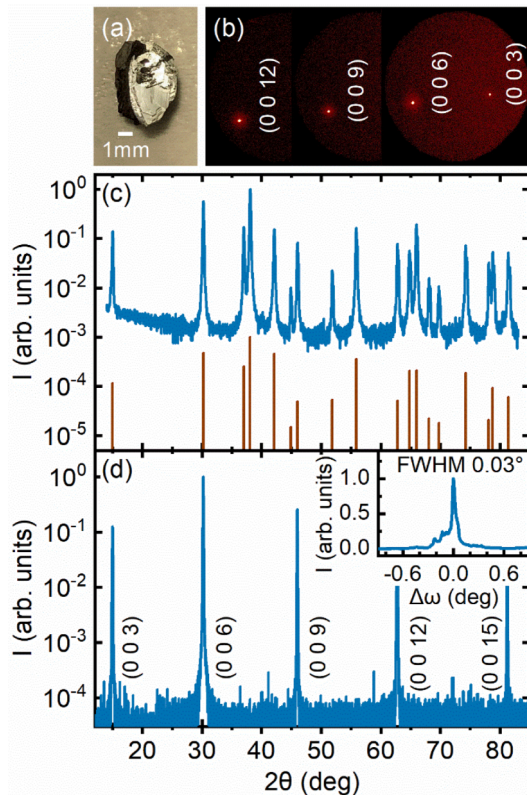
FIG. 3. (a) Photograph of a CVT-grown PdCoO$_2$ crystal with lateral size approximately 6×4 mm^2. (b) Two-dimensional detector images from 2D x-ray-diffraction measurements of a similar crystal, showing only 0 0 l reflections. (c) The 293 K powder x-ray-diffraction pattern from a powdered CVT crystal (blue), compared to a PdCoO$_2$ reference pattern (brown) [2,80]. (d) High-resolution wide-angle specular x-ray diffraction from a single crystal, showing only 0 0 l reflections. The inset to (d) is a high-resolution x-ray rocking curve through the 0 0 6 reflection in (d). The full width at half maximum of the primary peak is shown.

FIG. 4. (a) Low-temperature (12 K) powder x-ray-diffraction pattern from a powdered CVT PdCoO$_2$ crystal (black), along with a Rietveld refinement (blue). The difference between the experimental and refined curves is shown on a linear scale in pink below. (b) Temperature (T) dependence of the a (left axis) and c (right axis) lattice parameters from experiment (blue points) and DFT-based calculations (gold lines).

Figure 4(b) shows the $a(T)$ and $c(T)$ (blue points, left and right axes, respectively) extracted from Rietveld refinements at each T. Coarsely, the lattice parameters are relatively T independent up to $\sim$100 K, with approximately linear thermal expansion above $\sim$300 K. This is borne out more quantitatively by Fig. S2 in the Supplemental Material [75], which shows the T dependence of the a- and c-axis linear thermal expansion coefficients (α_{11} and α_{33}, respectively), obtained by numerical differentiation of the data in Fig. 4(b). The coefficients indeed increase with increasing T, leveling off at $\alpha_{11} \approx 9$ ppm K^{-1} and $\alpha_{33} \approx 7$ ppm K^{-1}. While we are not aware of any other thermal expansion data to compare to on *metallic* delafossites, these values are not far removed from those in CuAlO$_2$, for example, where $\alpha_{11} \approx 11$ ppm K^{-1} and $\alpha_{33} \approx 4$ ppm K^{-1} have been reported at 300 K and above [81]. Interestingly, Fig. S2 [75] provides evidence of a modest regime of negative c-axis thermal expansion (reaching ~ -0.5 ppm K^{-1}) below $\sim$100 K. This effect has been previously reported in a range of nonmetallic delafossites, particularly Cu-based ones, where it has been ascribed to anomalous contraction of Cu-O bonds [60,61].
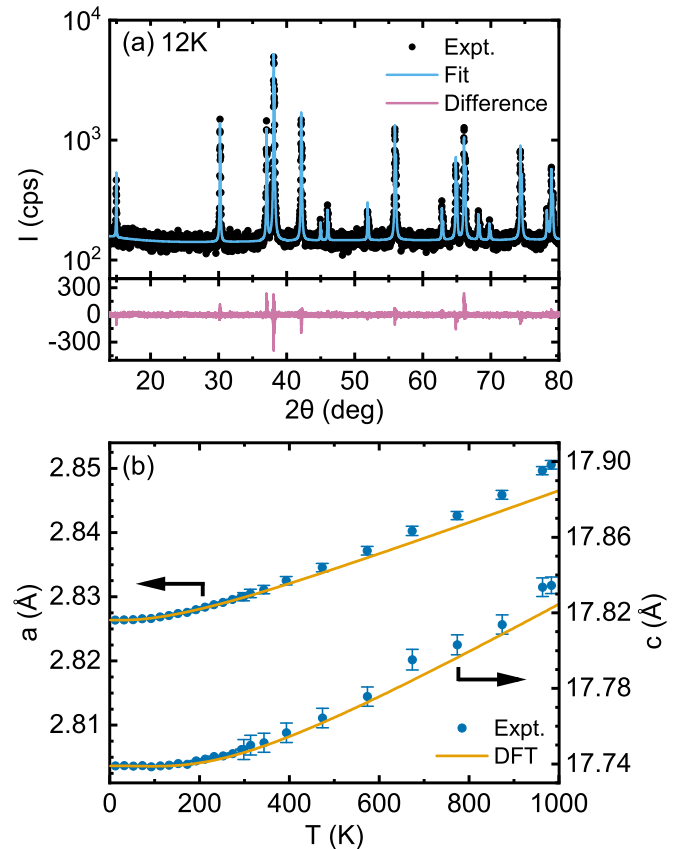
The gold-colored solid lines in Fig. 4(b) correspond to complementary DFT results for $a(T)$ and $c(T)$, obtained using the methods described in Sec. II. These are based on the quasiharmonic approximation, using fully relaxed structures and the Grüneisen theory of thermal expansion to calculate T-dependent thermal expansion coefficients (also shown in Fig. S2 [75]). The latter are then applied to the measured 12 K lattice parameters to generate the solid lines in Fig. 4(b). On the whole, the level of quantitative agreement between experiment and DFT is remarkably good in Figs. 4(b) and S2 [75], the only significant deviations occurring at the highest T. We note here that rapid ($\sim$20 K min^{-1}) cooling in air to room-temperature after acquiring the high-T data in Fig. 4(b) resulted in essentially identical a and c to initial crystals, ruling out irreversible changes due to defect (e.g., oxygen vacancy) formation. The modest differences between experiment and DFT at the highest T are thus likely not due to the onset of thermally induced nonstoichiometry; gradual breakdown of the quasiharmonic approximation used in the calculations is a more likely explanation. Aside from this, however, quantitative agreement between experiment and DFT calculations is achieved for the T-dependent structure and lattice parameters of PdCoO$_2$. This extends even to the small
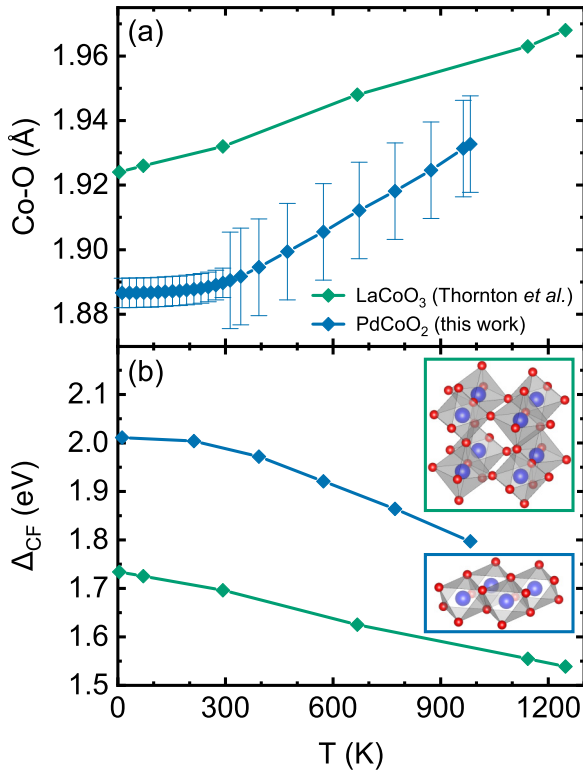
FIG. 5. Temperature (T) dependence of the Co-O bond length (a) and resulting DFT-calculated t_{2g}-e_g crystal field splitting [Δ_{CF}, (b)] in $PdCoO_2$ (this work) and $LaCoO_3$ (from Ref. [83]). The edge- and corner-shared octahedral environments in the two compounds are illustrated in (b); red ions are O, blue are Co.

range of negative c-axis thermal expansion below $\sim$100 K (Fig. S2 [75]).

Significantly, the above DFT calculations are based solely on lattice vibration effects, and do not include electronic excitations. It is thus apparently not necessary to account for, in particular, Co t_{2g} to e_g excitations that would induce a spin-state crossover from the low-spin ($S = 0$) state of the nominally Co^{3+} ions in $PdCoO_2$. While the Co-O octahedra in $PdCoO_2$ are edge shared [Fig. 1(a)], not corner shared, this finding is in contrast to many octahedrally coordinated Co^{3+}-containing cobaltites (e.g., the $RCoO_3$ perovskite series with R = La through Lu), which exhibit rich spin crossovers [52–59,82]. Insight into the origin of this contrasting behavior is obtained by comparing the Co-O bond lengths in such systems, which directly impact the crystal-field splitting of t_{2g} and e_g orbitals (Δ_{CF}), and thus the stability of the low-spin state [52–59,82]. Figure 5 achieves this by comparing the T dependence of the Co-O bond length in $PdCoO_2$ (from this work), with the archetypal perovskite cobaltite spin-crossover compound $LaCoO_3$ (from Thornton et al. [83]). The error bars on our Co-O bond lengths for $PdCoO_2$ are non-negligible here, due to the use of x-ray-rather than neutron diffraction, and some overlap of certain reflections with peaks due to the graphite dome on the heater stage at high T [84]. Nevertheless, the Co-O bond length is clearly shorter in $PdCoO_2$ than $LaCoO_3$ [83] (by > 0.03 Å at low T), the $PdCoO_2$ bond length reaching the low-T $LaCoO_3$ bond length only at the

highest T. Consistent with $a(T)$ and $c(T)$ in Fig. 4(b), the $PdCoO_2$ Co-O bond length is also free of the well-known anomalies in $LaCoO_3$ at the low-T and high-T spin-state crossover/transition. (The latter are already visible in the broad-T range data set of Thornton et al. [83] in Fig. 5(a) but are clearer in the dense data set of, e.g., Radaelli and Cheong [85].) Qualitatively, this comparison already points to stability of the low-spin state of the formally Co^{3+} ions in $PdCoO_2$, as the lower Co-O bond length should generate larger Δ_{CF}.

For further quantification, as discussed in Sec. II, we also used Wannier-function based tight-binding models to extract Δ_{CF} from DFT calculations of the electronic band structures of $PdCoO_2$ and $LaCoO_3$. This was done in a T-dependent manner, using our T-dependent experimental structural parameters. These multiorbital tight-binding models reproduce the DFT electronic structures essentially perfectly, through the use of a large number of parameters (see Fig. S3 in the Supplemental Material [75]). In addition to hopping parameters, these models also include an on-site energy for each orbital, corresponding to the average energy of the band induced by a given orbital, in the absence of interorbital mixing. These on-site energies can be used to estimate the trends in crystal-field levels for ions in similar environments. Since Co is octahedrally coordinated with O in both $PdCoO_2$ and $LaCoO_3$, we can use such on-site energies of the Co Wannier orbitals to estimate the Δ_{CF} between t_{2g} and e_g orbitals (see Fig. S3 and Table S1 in the Supplemental Material [75] for more details). Figure 5(b) plots the results, the low-T value of Δ_{CF} in $PdCoO_2$ exceeding that in $LaCoO_3$ by a significant $\sim$0.3 eV; this difference is maintained even at high T. With the competing Hund intra-atomic exchange energy likely to be very similar in the two compounds (this is a mostly atomic quantity, not strongly screened by the environment, and the two compounds share octahedral coordination), this substantially higher Δ_{CF} no doubt stabilizes the low-spin state of the formally Co^{3+} ions in $PdCoO_2$. We also calculated the effective valence of the nominally Co^{3+} ions in $PdCoO_2$ using bond-valence sums, based on our refined bond lengths. The result is a valence of +3.68 at low T, far larger than the nominal 3+ and the equivalent value in $LaCoO_3$, due to the short Co-O bonds. We interpret this substantial overbonding of the Co to result from inflexibility of the adjacent triangular Pd layers, where strong metallic bonds are understood to exist [26,33]. The connected Co-O octahedra are therefore unable to distort to relieve the overbonding of Co in the edge-shared octahedra. These findings significantly clarify the origin of the apparently rather stable low-spin state of the formally Co^{3+} ions in metallic delafossites such as $PdCoO_2$.

D. Specific-heat measurements

Measurements and analyses of $C_P(T)$ provide substantial further insight into the thermal properties of $PdCoO_2$. Shown first in Fig. 6(a) is the measured $C_P(T)$ of single-crystal $PdCoO_2$ (blue points) between 1.9 and 400 K, showing the expected monotonic increase, approaching $3R$ (R is the molar gas constant) above 400 K. (It is shown in Fig. S4 in Supplemental Material [75] that this overall $C_P(T)$ behavior is highly reproducible across multiple crystals.) Significantly, the DFT
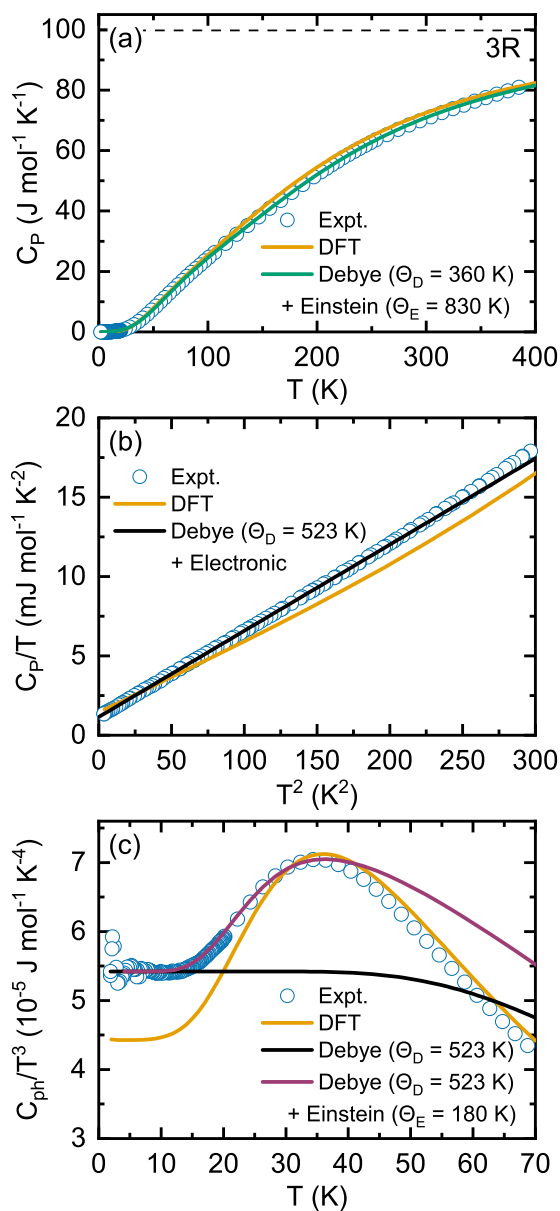
FIG. 6. (a) $PdCoO_2$ specific heat (C_P) vs temperature (T) from 1.9 to 400 K. Shown are experimental data (blue points), a DFT-based calculation (gold line), and the Debye-Einstein model described in the text (green line), with the shown Debye (Θ_D) and Einstein (Θ_E) temperatures. The Dulong-Petit $3R$ limit (R is the molar gas constant) is shown as a horizontal dashed line. (b) Low-temperature (2–17 K) C_P/T vs T^2 plot, showing experimental data (blue points), the DFT-based calculation (gold line), and a Debye plus Sommerfeld fit (black line, from 2 to 14 K) with $\Theta_D = 523$ K and $\gamma = 1.16$ mJ mol^{-1} K^{-2}. (c) Intermediate-temperature (2–70 K) C_{ph}/T^3 vs T plot, where C_{ph} is the phononic contribution to C_P, as determined by the methods described in the text. Shown are experimental data (blue points), the DFT-based calculation (gold line), the Debye model with $\Theta_D = 523$ K (*i.e.*, the value from the fit in (b)) (black line), and the Debye model with an additional Einstein mode with $\Theta_E = 180$ K (pink line).

calculations presented above, specifically the phonon DOS in Fig. 2(d), result in the gold-colored line in Fig. 6(a), revealing a remarkable level of agreement with the experimental $C_P(T)$. While this level of quantitative agreement is gratifying, it is nevertheless useful to apply commonly used simple models of specific heat to gain further insight into the *origin* of the agreement between experiment and theory. Following Takatsu *et al.* [15], the green line in Fig. 6(a) is thus a fit to a Debye-Einstein model, where a Debye term is used to capture the Pd- and Co-related phonon DOS, and an Einstein model is used to capture the higher-energy O-related phonon DOS, as depicted by the dashed lines in Fig. 2(d), and discussed in Sec. III A. This model amounts to [15,86–88]

$$C_P(T) = 9(1-X)NN_A k_B \left(\frac{T}{\Theta_D}\right)^3 \int_0^{\Theta_D/T} \frac{e^x x^4}{(e^x-1)^2}dx$$
$$+ 3XNN_A k_B \frac{e^{\Theta_E/T}}{(e^{\Theta_E/T}-1)^2}\left(\frac{\Theta_E}{T}\right)^2, \qquad (1)$$

where X is the weighting factor for the Einstein contribution ($1-X$ is thus the weight of the Debye contribution), N is the number of atoms per formula unit, N_A is Avogadro's number, k_B is Boltzmann's constant, and $x = \hbar\omega/k_B T$, where ω is the phonon frequency. The green-line fit to Eq. (1) in Fig. 6(a) is very good, confirming the validity of this approach and yielding $X = 0.59$, $\Theta_D = 360$ K, and $\Theta_E = 830$ K. Importantly, the latter temperatures are physically reasonable. Specifically, this high-T value of Θ_D is not only close to the prior report of Takatsu *et al.* [15] on $PdCoO_2$ (340 K), but also corresponds to $\omega_D = k_B\Theta_D/\hbar = 7.5$ THz, capturing the majority of the Co- and Pd-related phonon DOS in Fig. 2(d). Similarly, the high-T value of Θ_E is not only relatively close to the Takatsu *et al.* value (790 K [15]), but also corresponds to $\omega_E = k_B\Theta_E/\hbar = 17.5$ THz, close to the center of the high-frequency O-related optical modes in Fig. 2(d), which were also detected in Raman spectroscopy [15]. The close quantitative agreement between experiment and Eq. (1) in Fig. 6(a) thus derives from the ability of this form of Debye-Einstein model to reasonably capture the DFT-calculated phonon DOS in Fig. 2(d).

Further insight is obtained from the typical analysis of the low-T $C_P(T)$ for metallic systems, plotting C_P/T vs T^2 in Fig. 6(b). This is done to test for adherence to [86–88]

$$C_P(T) \approx \gamma T + 234NN_A k_B \left(\frac{T}{\Theta_D}\right)^3. \qquad (2)$$

This is simply the sum of the low-T approximations for the electronic and phononic contributions to $C_P(T)$ based on the Fermi liquid and Debye models (the high-ω_E Einstein oscillator discussed above is irrelevant at these low T) [86–88]. As illustrated by the black solid-line fit to Eq. (2), this form indeed describes the data well below $T^2 \approx 200$ K^2 (~14 K), resulting in $\gamma = 1.16$ mJ mol^{-1} K^{-2} and $\Theta_D = 523$ K. This γ is reasonably close to the Takatsu *et al.* [15] value of

1.28 mJ mol^{-1} K^{-2} but substantially smaller than the Tanaka *et al.* [62] value of 4.14 mJ mol^{-1} K^{-2}, which, as noted in Sec. I, was obtained on relatively low-quality PdCoO$_2$ crystals with a prominent Schottky anomaly in $C_P(T)$ [of which there is no indication in Fig. 6(b)]. More importantly, as illustrated by the gold-colored line in Fig. 6(b), our DFT calculations yield a quite similar γ of 1.45 mJ mol^{-1} K^{-2}, establishing reasonable quantitative agreement with the near-E_F DOS in Fig. 2(b). These values are also in good agreement with other DFT calculations (0.9–1.8 mJ mol^{-1} K^{-2} based on published DOS values at E_F [26,27,30]) and experimental measurements ($\sim$1 mJ mol^{-1} K^{-2} calculated from de Haas–van Alphen data [16], and $\sim$1.5 mJ mol^{-1} K^{-2} calculated from angle-resolved photoemission spectroscopy [19,89]). In terms of the extracted low-T Θ_D of 523 K, this is also in reasonable agreement with the low-T Θ_D of 501 K from Takatsu *et al.* [15], the significant deviation from the higher-T Θ_D being quite common in Debye-model based analysis of $C_P(T)$ [86–88]. We note that it is this Θ_D value that is used to plot the Debye-model phonon DOS in Fig. 2(d). In principle, comparisons of the above Debye temperatures to those in other (insulating) delafossites could be insightful, but the latter appear to be widely scattered in the literature, in the 400–800 K range [90–96]. This is likely related to the fact that experimental determinations have been performed over quite different T ranges, in some cases after subtraction of substantial magnetic contributions to C_P.

While Figs. 6(a) and 6(b) thus reveal good agreement with high-T Debye-Einstein and low-T Debye-Sommerfeld modeling, respectively [i.e., Eqs. (1) and (2)], our experimental single-crystal PdCoO$_2$ $C_P(T)$ data do reveal one significant departure from simple model behavior, as highlighted in Fig. 6(c). This figure plots the experimental C_{ph}/T^3 vs T, where $C_{ph}(T)$ is the phononic part of $C_P(T)$, isolated by subtracting the experimental γT electronic contribution established from the analysis in Fig. 6(b). Based on Eq. (2), the data in Fig. 6(c) should be essentially horizontal if the Debye model is entirely adhered to at low T, with an intercept on the C_{ph}/T^3 axis dictated by Θ_D [63]. At higher T, downward deviations would then be expected as the limits of applicability of the T^3 Debye model approximation in Eq. (2) are exceeded, as for the black line, which is the Debye model result based on $\Theta_D = 523$ K. The experimental data in Fig. 6(c) clearly depart from this expectation, however: C_{ph}/T^3 is flat at the lowest T, but only below $\sim$15 K, above which a clear peak emerges, centered at $\sim$35 K. As illustrated by the gold and black lines, respectively, DFT calculations of $C_{ph}(T)$ capture this peak (albeit with the small departure from the experimental low-T Θ_D that is discussed below), while Eq. (2) does not. The pink line in Fig. 6(c) shows that the bulk of this discrepancy between Eq. (2) and the experimental data can be resolved by adding a single Einstein mode with $\Theta_E = 180$ K to the low-T Debye model. We stress that this Einstein mode is clearly distinct from the one with $\Theta_E = 830$ K used to capture the high-frequency O-related modes in Fig. 2(d), as needed to model the high-T $C_P(T)$ in Fig. 6(a). On the contrary, $\Theta_E = 180$ K corresponds to $\omega_E = k_B\Theta_E/\hbar = 3.8$ THz, closely matching the first (i.e., lowest-energy) peaks in the phonon DOS in Fig. 2(d). This is a known phenomenon in per-

ovskite oxides, for example (such as SrTiO$_3$ [63]), arising due to a peak phonon DOS exceeding the Debye model description [compare the total DOS and Debye model dashed line in Fig. 2(d)], thus generating excess intermediate-T phononic specific heat. We thus believe that it is reasonable for PdCoO$_2$ to exhibit such an effect, particularly given the common Co-O octahedral structural units, and it is reassuring that this is indeed captured by DFT [compare the blue points and gold line in Fig. 6(c)]. For completeness, we note that adding the low-Θ_E Einstein mode to the overall fit to the entire $C_P(T)$ dataset with Eq. (1) shifts Θ_D and the higher-Θ_E value from 360 and 830 K, respectively, to 390 and 890 K, respectively. These are modest shifts of approximately 8 and 7%, respectively.

While, from the above, the overall level of quantitative agreement between experiment and DFT calculations on $C_P(T)$ in PdCoO$_2$ is impressive, the discrepancy between the low-T Θ_D from experiment (523 K) and DFT (556 K) is worthy of further discussion. This is most readily apparent in Fig. 6(c) (from the difference in the low-T asymptotic values), but can also be seen in Fig. 6(b) upon close inspection (from the small difference in low-T slope). We first note that this $\sim$6% difference in Θ_D is quite modest on absolute terms. One likely source of this discrepancy, however, is the $2 \times 2 \times 2$ supercell used for the DFT phonon calculations, which necessarily limits the accuracy of the low-energy/long-wavelength phonon DOS calculation. We thus repeated calculations using a $3 \times 3 \times 3$ supercell, which indeed brings the low-frequency DOS closer to that of the Debye model with the experimental low-T Θ_D of 523 K, as shown in Fig. S5, with little impact on the higher-frequency band structure and DOS (Fig. S6). We also checked that these results are independent of the k-space mesh spacing used in the calculations. From the resulting calculated $C_P(T)$, the low-T Θ_D value is 516 K, significantly closer to the experimental value of 523 K. We thus conclude a high level of quantitative agreement between experiment and first-principles calculations in essentially all aspects of the thermal behavior probed in this work.

IV. SUMMARY

In summary, this work has combined DFT-based calculations of the electronic and phononic structures of the model delafossite metal PdCoO$_2$ with single-crystal measurements of wide-temperature range thermal properties, encompassing crystal structure, thermal expansion, and specific heat. The $R\bar{3}m$ space group is maintained over essentially the entire temperature range prior to PdCoO$_2$ decomposition (certainly 12–1000 K), confirming the stability of the 3R delafossite polymorph. Aside from a small region of negative thermal expansion, quite typical thermal expansion is observed along the a- and c-axes, with magnitudes in quantitative agreement with phonon-based DFT calculations. The absence of electronic excitation effects in such data imply strong stability of the low-spin ($S = 0$) state of the formally Co^{3+} ions, which we have explicitly elucidated by comparing temperature-dependent Co-O bond lengths and crystal–field splittings in PdCoO$_2$ and LaCoO$_3$. Complementary specific heat data are

also in excellent agreement with DFT calculations, both in terms of electronic and phononic contributions. Insight into the origins of this agreement is provided by Debye-Einstein modeling, establishing that the DFT-calculated phonon DOS can be described by a Debye model capturing the lower-frequency Co- and Pd-related DOS and an Einstein model capturing the quite unusual high-frequency O-related optical modes. DFT additionally captures intermediate-temperature excess specific heat over simple Debye modeling, an effect related to the first (i.e., lowest-energy) peaks in the phonon DOS, as observed in perovskite oxides. In totality, we thus claim quantitative understanding of key thermal properties of $PdCoO_2$, thereby significantly advancing the overall under-standing of the metallic delafossites that have generated such substantial recent interest.

[1] R. D. Shannon, D. B. Rogers, and C. T. Prewitt, Chemistry of noble metal oxides. I. Syntheses and properties of ABO_2 delafossite compounds, Inorg. Chem. **10**, 713 (1971).

[2] C. T. Prewitt, R. D. Shannon, and D. B. Rogers, Chemistry of noble metal oxides. II. Crystal structures of platinum cobalt dioxide, palladium cobalt dioxide, copper iron dioxide, and silver iron dioxide, Inorg. Chem. **10**, 719 (1971).

[3] D. B. Rogers, R. D. Shannon, C. T. Prewitt, and J. L. Gillson, Chemistry of noble metal oxides. III. Electrical transport properties and crystal chemistry of ABO_2 compounds with the delafossite structure, Inorg. Chem. **10**, 723 (1971).

[4] A. P. Mackenzie, The properties of ultrapure delafossite metals, Rep. Prog. Phys. **80**, 032501 (2017).

[5] M. Mekata, N. Yaguchi, T. Takagi, S. Mitsuda, and H. Yoshizawa, Magnetic ordering in delafossite $CuFeO_2$, J. Magn. Magn. Mater. **104–107**, 823 (1992).

[6] S. Mitsuda, H. Yoshizawa, N. Yaguchi, and M. Mekata, Neutron diffraction study of $CuFeO_2$, J. Phys. Soc. Jpn. **60**, 1885 (1991).

[7] F. Ye, J. A. Fernandez-Baca, R. S. Fishman, Y. Ren, H. J. Kang, Y. Qiu, and T. Kimura, Magnetic Interactions in the Geometrically Frustrated Triangular Lattice Antiferromagnet $CuFeO_2$, Phys. Rev. Lett. **99**, 157201 (2007).

[8] S. Mitsuda, N. Kasahara, T. Uno, and M. Mase, Partially disordered phase in frustrated triangular lattice antiferromagnet $CuFeO_2$, J. Phys. Soc. Jpn. **67**, 4026 (1998).

[9] M. Yu, G. Natu, Z. Ji, and Y. Wu, P-Type dye-sensitized solar cells based on delafossite $CuGaO_2$ nanoplates with saturation photovoltages exceeding 460 mv, J. Phys. Chem. Lett. **3**, 1074 (2012).

[10] W. A. Dunlap-Shohl, T. B. Daunis, X. Wang, J. Wang, B. Zhang, D. Barrera, Y. Yan, J. W. P. Hsu, and D. B. Mitzi, Room-temperature fabrication of a delafossite $CuCrO_2$ hole transport layer for perovskite solar cells, J. Mater. Chem. A **6**, 469 (2018).

[11] A. P. Amrute, G. O. Larrazábal, C. Mondelli, and J. Pérez-Ramírez, $CuCrO_2$ delafossite: A stable copper catalyst for chlorine production, Angew. Chem. Int. Ed. **52**, 9772 (2013).

[12] K. Toyoda, R. Hinogami, N. Miyata, and M. Aizawa, Calculated descriptors of catalytic activity for water electrolysis anode: Application to delafossite oxides, J. Phys. Chem. C **119**, 6495 (2015).

[13] R. Daou, R. Frésard, V. Eyert, S. Hébert, and A. Maignan, Unconventional aspects of electronic transport in delafossite oxides, Sci. Technol. Adv. Mater. **18**, 919 (2017).

[14] N. Nandi, T. Scaffidi, P. Kushwaha, S. Khim, M. E. Barber, V. Sunko, F. Mazzola, P. D. C. King, H. Rosner, P. J. W. Moll, M. König, J. E. Moore, S. Hartnoll, and A. P. Mackenzie, Unconventional magneto-transport in ultrapure $PdCoO_2$ and $PtCoO_2$, npj Quantum Mater. **3**, 66 (2018).

[15] H. Takatsu, S. Yonezawa, S. Mouri, S. Nakatsuji, K. Tanaka, and Y. Maeno, Roles of high-frequency optical phonons in the physical properties of the conductive delafossite $PdCoO_2$, J. Phys. Soc. Jpn. **76**, 104701 (2007).

[16] C. W. Hicks, A. S. Gibbs, A. P. Mackenzie, H. Takatsu, Y. Maeno, and E. A. Yelland, Quantum Oscillations and High Carrier Mobility in the Delafossite $PdCoO_2$, Phys. Rev. Lett. **109**, 116401 (2012).

[17] C. S. Chang, J. Sun, S. Khim, A. P. Mackenzie, D. G. Schlom, and D. A. Muller, Visualization of defects in single-crystal and thin-film $PdCoO_2$ using aberration-corrected scanning transmission electron microscopy, Phys. Rev. Mater. **6**, 093401 (2022).

[18] V. Sunko, P. H. McGuinness, C. S. Chang, E. Zhakina, S. Khim, C. E. Dreyer, M. Konczykowski, H. Borrmann, P. J. W. Moll, M. König, D. A. Muller, and A. P. Mackenzie, Controlled Introduction of Defects to Delafossite Metals by Electron Irradiation, Phys. Rev. X **10**, 021018 (2020).

[19] H.-J. Noh, J. Jeong, J. Jeong, E.-J. Cho, S. B. Kim, K. Kim, B. I. Min, and H.-D. Kim, Anisotropic Electric Conductivity of Delafossite $PdCoO_2$ Studied by Angle-Resolved Photoemission Spectroscopy, Phys. Rev. Lett. **102**, 256404 (2009).

[20] P. Kushwaha, V. Sunko, P. J. W. Moll, L. Bawden, J. M. Riley, N. Nandi, H. Rosner, M. P. Schmidt, F. Arnold, E. Hassinger, T. K. Kim, M. Hoesch, A. P. Mackenzie, and P. D. C. King, Nearly free electrons in a 5d delafossite oxide metal, Sci. Adv. **1**, e1500692 (2022).

[21] V. Sunko, H. Rosner, P. Kushwaha, S. Khim, F. Mazzola, L. Bawden, O. J. Clark, J. M. Riley, D. Kasinathan, M. W. Haverkort, T. K. Kim, M. Hoesch, J. Fujii, I. Vobornik, A. P. Mackenzie, and P. D. C. King, Maximal Rashba-like spin splitting via kinetic-energy-coupled inversion-symmetry breaking, Nature (London) **549**, 492 (2017).

[22] F. Mazzola, V. Sunko, S. Khim, H. Rosner, P. Kushwaha, O. J. Clark, L. Bawden, I. Marković, T. K. Kim, M. Hoesch, A. P.

Mackenzie, and P. D. C. King, Itinerant ferromagnetism of the Pd-terminated polar surface of $PdCoO_2$, Proc. Natl. Acad. Sci. **115**, 12956 (2018).

[23] P. J. W. Moll, P. Kushwaha, N. Nandi, B. Schmidt, and A. P. Mackenzie, Evidence for hydrodynamic electron flow in $PdCoO_2$, Science **351**, 1061 (2016).

[24] C. Putzke, M. D. Bachmann, P. McGuinness, E. Zhakina, V. Sunko, M. Konczykowski, T. Oka, R. Moessner, A. Stern, M. König, S. Khim, A. P. Mackenzie, and P. J. W. Moll, h/e oscillations in interlayer transport of delafossites, Science **368**, 1234 (2020).

[25] V. Eyert, R. Frésard, and A. Maignan, On the metallic conductivity of the delafossites $PdCoO_2$ and $PtCoO_2$, Chem. Mater. **20**, 2370 (2008).

[26] K. P. Ong, J. Zhang, J. S. Tse, and P. Wu, Origin of anisotropy and metallic behavior in delafossite $PdCoO_2$, Phys. Rev. B **81**, 115120 (2010).

[27] S. Kumar, H. C. Gupta, and Karandeep, First principles study of structural, bonding and vibrational properties of $PtCoO_2$, $PdCoO_2$ and $PdRhO_2$ metallic delafossites, J. Phys. Chem. Solids **74**, 305 (2013).

[28] K. Kim, H. C. Choi, and B. I. Min, Fermi surface and surface electronic structure of delafossite $PdCoO_2$, Phys. Rev. B **80**, 035116 (2009).

[29] K. P. Ong, D. J. Singh, and P. Wu, Unusual Transport and Strongly Anisotropic Thermopower in $PtCoO_2$ and $PdCoO_2$, Phys. Rev. Lett. **104**, 176601 (2010).

[30] M. E. Gruner, U. Eckern, and R. Pentcheva, Impact of strain-induced electronic topological transition on the thermoelectric properties of $PtCoO_2$ and $PdCoO_2$, Phys. Rev. B **92**, 235140 (2015).

[31] F. Lechermann, From basic properties to the Mott design of correlated delafossites, npj Comput. Mater. **7**, 120 (2021).

[32] H. Usui, M. Ochi, S. Kitamura, T. Oka, D. Ogura, H. Rosner, M. W. Haverkort, V. Sunko, P. D. C. King, A. P. Mackenzie, and K. Kuroki, Hidden Kagome-lattice picture and origin of high conductivity in delafossite $PtCoO_2$, Phys. Rev. Mater. **3**, 045002 (2019).

[33] M. Tanaka, M. Hasegawa, and H. Takei, Growth and anisotropic physical properties of $PdCoO_2$ single crystals, J. Phys. Soc. Jpn. **65**, 3973 (1996).

[34] M. Itoh, M. Mori, M. Tanaka, and H. Takei, NMR study of two-dimensional itinerant magnets $PtCoO_2$ and $PdCoO_2$ with a triangular lattice, Phys. B **259–261**, 999 (1999).

[35] H. Takatsu, J. J. Ishikawa, S. Yonezawa, H. Yoshino, T. Shishidou, T. Oguchi, K. Murata, and Y. Maeno, Extremely Large Magnetoresistance in the Nonmagnetic Metal $PdCoO_2$, Phys. Rev. Lett. **111**, 056601 (2013).

[36] M. D. Bachmann, A. L. Sharpe, A. W. Barnard, C. Putzke, M. König, S. Khim, D. Goldhaber-Gordon, A. P. Mackenzie, and P. J. W. Moll, Super-geometric electron focusing on the hexagonal Fermi surface of $PdCoO_2$, Nat. Commun. **10**, 5081 (2019).

[37] T. Harada, K. Sugawara, K. Fujiwara, M. Kitamura, S. Ito, T. Nojima, K. Horiba, H. Kumigashira, T. Takahashi, T. Sato, and A. Tsukazaki, Anomalous Hall effect at the spontaneously electron-doped polar surface of $PdCoO_2$ ultrathin films, Phys. Rev. Res. **2**, 013282 (2020).

[38] F. Mazzola, C. -M. Yim, V. Sunko, S. Khim, P. Kushwaha, O. J. Clark, L. Bawden, I. Marković, D. Chakraborti, T. K. Kim, M.

Hoesch, A. P. Mackenzie, P. Wahl, and P. D. C. King, Tuneable electron–magnon coupling of ferromagnetic surface states in $PdCoO_2$, npj Quantum Mater. **7**, 20 (2022).

[39] T. Harada, K. Fujiwara, and A. Tsukazaki, Highly conductive $PdCoO_2$ ultrathin films for transparent electrodes, APL Mater. **6**, 046107 (2018).

[40] P. Yordanov, A. S. Gibbs, P. Kaya, S. Bette, W. Xie, X. Xiao, A. Weidenkaff, H. Takagi, and B. Keimer, High-temperature electrical and thermal transport properties of polycrystalline $PdCoO_2$, Phys. Rev. Mater. **5**, 015404 (2021).

[41] R. Wei, P. Gong, M. Zhao, H. Tong, X. Tang, L. Hu, J. Yang, W. Song, X. Zhu, and Y. Sun, Solution-processable epitaxial metallic delafossite oxide films, Adv. Funct. Mater. **30**, 2002375 (2020).

[42] J. Sun, M. R. Barone, C. S. Chang, M. E. Holtz, H. Paik, J. Schubert, D. A. Muller, and D. G. Schlom, Growth of $PdCoO_2$ by ozone-assisted molecular-beam epitaxy, APL Mater. **7**, 121112 (2019).

[43] Q. Song, J. Sun, C. T. Parzyck, L. Miao, Q. Xu, F. V. E. Hensling, M. R. Barone, C. Hu, J. Kim, B. D. Faeth, H. Paik, P. D. C. King, K. M. Shen, and D. G. Schlom, Growth of $PdCoO_2$ films with controlled termination by molecular-beam epitaxy and determination of their electronic structure by angle-resolved photoemission spectroscopy, APL Mater. **10**, 91113 (2022).

[44] T. Harada, Thin-film growth and application prospects of metallic delafossites, Mater. Today Adv. **11**, 100146 (2021).

[45] T. Harada, S. Ito, and A. Tsukazaki, Electric dipole effect in $PdCoO_2/\beta$-Ga_2O_3 Schottky diodes for high-temperature operation, Sci. Adv. **5**, eaax5733 (2019).

[46] T. Harada and Y. Okada, Metallic delafossite thin films for unique device applications, APL Mater. **10**, 70902 (2022).

[47] M. Brahlek, G. Rimal, J. M. Ok, D. Mukherjee, A. R. Mazza, Q. Lu, H. N. Lee, T. Z. Ward, R. R. Unocic, G. Eres, and S. Oh, Growth of metallic delafossite $PdCoO_2$ by molecular beam epitaxy, Phys. Rev. Mater. **3**, 093401 (2019).

[48] J. M. Ok, M. Brahlek, W. S. Choi, K. M. Roccapriore, M. F. Chisholm, S. Kim, C. Sohn, E. Skoropata, S. Yoon, J. S. Kim, and H. N. Lee, Pulsed-laser epitaxy of metallic delafossite $PdCrO_2$ films, APL Mater. **8**, 051104 (2020).

[49] J. M. Ok, S. Yoon, A. R. Lupini, P. Ganesh, A. Huon, M. F. Chisholm, and H. N. Lee, Twin-domain formation in epitaxial triangular lattice delafossites, ACS Appl. Mater. Interfaces **13**, 22059 (2021).

[50] J. M. Ok, S. Yoon, A. R. Lupini, P. Ganesh, M. F. Chisholm, and H. N. Lee, Interfacial stabilization for epitaxial $CuCrO_2$ delafossites, Sci. Rep. **10**, 11375 (2020).

[51] P. Yordanov, W. Sigle, P. Kaya, M. E. Gruner, R. Pentcheva, B. Keimer, and H.-U. Habermeier, Large thermopower anisotropy in $PdCoO_2$ thin films, Phys. Rev. Mater. **3**, 085403 (2019).

[52] M. Imada, A. Fujimori, and Y. Tokura, Metal-insulator transitions, Rev. Mod. Phys. **70**, 1039 (1998).

[53] R. R. Heikes, R. C. Miller, and R. Mazelsky, Magnetic and electrical anomalies in $LaCoO_3$, Physica **30**, 1600 (1964).

[54] P. M. Raccah and J. B. Goodenough, First-order localized-electron ⇆ collective-electron transition in $LaCoO_3$, Phys. Rev. **155**, 932 (1967).

[55] M. A. Korotin, S. Yu. Ezhov, I. V. Solovyev, V. I. Anisimov, D. I. Khomskii, and G. A. Sawatzky, Intermediate-spin state and properties of $LaCoO_3$, Phys. Rev. B **54**, 5309 (1996).

[56] A. Podlesnyak, S. Streule, J. Mesot, M. Medarde, E. Pom-jakushina, K. Conder, A. Tanaka, M. W. Haverkort, and D. I. Khomskii, Spin-State Transition in LaCoO$_3$: Direct Neutron Spectroscopic Evidence of Excited Magnetic States, Phys. Rev. Lett. **97**, 247208 (2006).

[57] M. W. Haverkort, Z. Hu, J. C. Cezar, T. Burnus, H. Hartmann, M. Reuther, C. Zobel, T. Lorenz, A. Tanaka, N. B. Brookes, H. H. Hsieh, H.-J. Lin, C. T. Chen, and L. H. Tjeng, Spin State Transition in LaCoO$_3$ Studied Using Soft X-Ray Absorption Spectroscopy and Magnetic Circular Dichroism, Phys. Rev. Lett. **97**, 176405 (2006).

[58] Z. Ropka and R. J. Radwanski, ^{5}D term origin of the excited triplet in LaCoO$_3$, Phys. Rev. B **67**, 172401 (2003).

[59] R. F. Klie, J. C. Zheng, Y. Zhu, M. Varela, J. Wu, and C. Leighton, Direct Measurement of the Low-Temperature Spin-State Transition in LaCoO$_3$, Phys. Rev. Lett. **99**, 047203 (2007).

[60] J. Li, A. W. Sleight, C. Y. Jones, and B. H. Toby, Trends in negative thermal expansion behavior for AMO$_2$ (A=Cu or Ag; M=Al, Sc, In, or La) compounds with the delafossite structure, J. Solid State Chem. **178**, 285 (2005).

[61] J. Li, A. Yokochi, T. G. Amos, and A. W. Sleight, Strong negative thermal expansion along the O-Cu-O linkage in CuScO$_2$, Chem. Mater. **14**, 2602 (2002).

[62] M. Tanaka, M. Hasegawa, T. Higuchi, T. Tsukamoto, Y. Tezuka, S. Shin, and H. Takei, Origin of the Metallic Conductivity in PdCoO$_2$ with Delafossite Structure, Phys. B: Condens. Matter **245**, 157 (1998)

[63] E. McCalla, M. N. Gastiasoro, G. Cassuto, R. M. Fernandes, and C. Leighton, Low-temperature specific heat of doped SrTiO$_3$: Doping dependence of the effective mass and Kadowaki-Woods scaling violation, Phys. Rev. Mater. **3**, 022001(R) (2019).

[64] M. Binnewies, R. Glaum, M. Schmidt, and P. Schmidt, *Chemical Vapor Transport Reactions* (De Gruyter, Berlin, 2012).

[65] Y. Zhang, F. Tutt, G. Evans, B. Kaiser, J. Ramberger, G. Haugstad, W. Seyfried, and C. Leighton (unpublished).

[66] J. C. Lashley, M. F. Hundley, A. Migliori, J. L. Sarrao, P. G. Pagliuso, T. W. Darling, M. Jaime, J. C. Cooley, W. L. Hults, L. Morales, D. J. Thoma, J. L. Smith, J. Boerio-Goates, B. F. Woodfield, G. R. Stewart, R. A. Fisher, and N. E. Phillips, Critical examination of heat capacity measurements made on a quantum design physical property measurement system, Cryogenics **43**, 369 (2003).

[67] G. Kresse and J. Furthmüller, Efficiency of ab-initio total energy calculations for metals and semiconductors using a plane-wave basis set, Comput. Mater. Sci. **6**, 15 (1996).

[68] G. Kresse and J. Furthmüller, Efficient iterative schemes for ab initio total-energy calculations using a plane-wave basis set, Phys. Rev. B **54**, 11169 (1996).

[69] J. P. Perdew, A. Ruzsinszky, G. I. Csonka, O. A. Vydrov, G. E. Scuseria, L. A. Constantin, X. Zhou, and K. Burke, Restoring the Density-Gradient Expansion for Exchange in Solids and Surfaces, Phys. Rev. Lett. **100**, 136406 (2008).

[70] H. J. Monkhorst and J. D. Pack, Special points for Brillouin-zone integrations, Phys. Rev. B **13**, 5188 (1976).

[71] A. A. Mostofi, J. R. Yates, Y.-S. Lee, I. Souza, D. Vanderbilt, and N. Marzari, Wannier90: A tool for obtaining maximally-localised Wannier functions, Comput. Phys. Commun. **178**, 685 (2008).

[72] N. Marzari, A. A. Mostofi, J. R. Yates, I. Souza, and D. Vanderbilt, Maximally localized Wannier functions: Theory and applications, Rev. Mod. Phys. **84**, 1419 (2012).

[73] A. Togo and I. Tanaka, First principles phonon calculations in materials science, Scr. Mater. **108**, 1 (2015).

[74] E. T. Ritz, S. J. Li, and N. A. Benedek, Thermal expansion in insulating solids from first principles, J. Appl. Phys. **126**, 171102 (2019).

[75] See Supplemental Material at http://link.aps.org/supplemental/10.1103/PhysRevMaterials.6.115004 for additional Information on phonon band- structure calculations; thermal expansion coefficients; the electronic band structure of; crystal-field splitting energies; specific-heat measurements on multiple crystals; and comparisons of phonon calculations with different size supercells.

[76] K. M. Rabe, M. Dawber, C. Lichtensteiger, C. H. Ahn, and J.-M. Triscone, *Physics of Ferroelectrics: A Modern Perspective* (Springer, Berlin, 2007).

[77] P. Ghosez, E. Cockayne, U. V. Waghmare, and K. M. Rabe, Lattice dynamics of BaTiO$_3$, PbTiO$_3$, and PbZrO$_3$: A comparative first-principles study, Phys. Rev. B **60**, 836 (1999).

[78] B. Klobes, M. Herlitschke, K. Z. Rushchanskii, H.-C. Wille, T. T. A. Lummen, P. H. M. van Loosdrecht, A. A. Nugroho, and R. P. Hermann, Anisotropic lattice dynamics and intermediate-phase magnetism in delafossite CuFeO$_2$, Phys. Rev. B **92**, 014304 (2015).

[79] D. Bansal, J. L. Niedziela, A. F. May, A. Said, G. Ehlers, D. L. Abernathy, A. Huq, M. Kirkham, H. Zhou, and O. Delaire, Lattice dynamics and thermal transport in multiferroic CuCrO$_2$, Phys. Rev. B **95**, 054306 (2017).

[80] PdCoO$_2$ (CoPdO$_2$) crystal structure: Datasheet, *PAULING FILE in Inorganic Solid Phases, Springer Materials (online database)*, Dataset ID sd_1920856 (Springer, Heidelberg, 2016).

[81] T. Ishiguro, N. Ishizawa, N. Mizutani, and M. Kato, High temperature structural investigation of the delafossite type compound CuAlO$_2$, J. Solid State Chem. **41**, 132 (1982).

[82] M. Tachibana, T. Yoshida, H. Kawaji, T. Atake, and E. Takayama-Muromachi, Evolution of electronic states in *R*CoO$_3$ (R = rare earth): Heat capacity measurements, Phys. Rev. B **77**, 094402 (2008).

[83] G. Thornton, B. C. Tofield, and A. W. Hewat, A neutron diffraction study of LaCoO$_3$ in the temperature range $4.2 < T < 1248$ K, J. Solid State Chem. **61**, 301 (1986).

[84] Our Rietveld-refined O$_z$ coordinates were determined with relatively low precision as a function of *T*, particularly at higher *T*, due to these factors. We thus fitted the entire O$_z$ coordinate vs *T* dataset and used the resulting fit in conjunction with $a(T)$ and $c(T)$ to generate the Co-O bond length data in Fig. 5(a). Without this procedure, the bond-length data retain the same overall behavior as in Fig. 5(a), but with additional scatter.

[85] P. G. Radaelli and S.-W. Cheong, Structural phenomena associated with the spin-state transition in LaCoO$_3$, Phys. Rev. B **66**, 094408 (2002).

[86] C. Kittel, *Introduction to Solid State Physics*, 8th ed. (John Wiley & Sons, New York, 2005).

[87] E. S. R. Gopal, *Specific Heats at Low Temperatures* (Springer, New York, 1966).

[88] H. M. Rosenberg, *Low Temperature Solid State Physics* (Oxford University Press, New York, 1963).

[89] V. Sunko, Ph.D. thesis: Angle Resolved Photoemission Spectroscopy of Delafossite Metals, Max Planck Institute for Chemical Physics of Solids (2019).

[90] O. J. Durá, R. Boada, A. Rivera-Calzada, C. León, E. Bauer, M. A. L. de la Torre, and J. Chaboy, Transport, electronic, and structural properties of nanocrystalline $CuAlO_2$ delafossites, Phys. Rev. B **83**, 045202 (2011).

[91] E. A. Zvereva, M. I. Stratan, A. V. Ushakov, V. B. Nalbandyan, I. L. Shukaev, A. V. Silhanek, M. Abdel-Hafiez, S. V. Streltsov, and A. N. Vasiliev, Orbitally induced hierarchy of exchange interactions in the zigzag antiferromagnetic state of honeycomb silver delafossite $Ag_3Co_2SbO_6$, Dalton Trans. **45**, 7373 (2016).

[92] Y. Haraguchi, K. Kakimoto, and H. A. Katori, $4d^3$ Ru^{5+} triangular lattice Antiferromagnets: Layered rock-salt β-$Li_3Mg_2RuO_6$ and ion-exchanged delafossite $Ag_3Mg_2RuO_6$, J. Solid State Chem. **299**, 122171 (2021).

[93] M. K. Majee, P. A. Bhobe, and A. K. Nigam, Griffiths phase in antiferromagnetic $CuCr_{0.95}Ti_{0.05}O_2$, J. Magn. Magn. Mater. **485**, 112 (2019).

[94] A. Ababou, F. Chiker, H. Khachai, R. Miloua, R. Khenata, R. Ahmed, S. H. Naqib, A. Bouhemadou, S. Bin Omran, F. Boukabrine, and X. Wang, DFT-based computer simulation of the physical properties of transparent conducting oxide of delafossite-type: $AgInO_2$ and $AgYO_2$, Phys. B: Condens. Matter **601**, 412584 (2021).

[95] D. M. Hoat, Theoretical study of electronic structure, thermoelectric and thermodynamic properties of 2H-$AgAlO_2$, Phys. B: Condens. Matter **558**, 109 (2019).

[96] Q.-J. Liu, Z.-T. Liu, and L.-P. Feng, Theoretical calculations of mechanical, electronic, chemical bonding and optical properties of delafossite $CuAlO_2$, Phys. B: Condens. Matter **405**, 2028 (2010).

[97] K. Momma and F. Izumi, VESTA3 for three-dimensional visualization of crystal, volumetric and morphology data, J. Appl. Crystallogr. **44**, 1272 (2011).

[98] A. Kokalj, Computer graphics and graphical user interfaces as tools in simulations of matter at the atomic scale, Comput. Mater. Sci. **28**, 155 (2003).

Correction: The previously published Figure 2 contained an error in the plot of the lower dashed line in panel (d) and has been replaced.